

Illumination Compensation via Inverted Dehazing. Applications on Retinal and Skin Imaging

Adrian Galdran*, Artzai Picon, Aitor Alvarez-Gila, Alessandro Bria,
Claudio Marrocco, Mario Molinara, Francesco Tortorella, and Aurélio Campilho

Abstract—The effective compensation of irregular illumination remains a challenging problem in biomedical imaging. Due to different physical phenomena taking place during the acquisition or image formation process, inhomogeneous illumination fields affect the quality of the visual information, decreasing visibility of anatomical structures, hindering interpretability and affecting the performance of subsequent computer vision tasks. In this work, we draw a theoretical connection between illumination compensation and the apparently unrelated problem of image dehazing, consisting of removing fog from weather-degraded outdoor images. Namely, while the presence of an uneven illumination field may drive image intensities towards low values, the presence of fog produces an inverse effect, saturating intensity towards white. We thus propose to apply image dehazing techniques on images affected by under-exposure, after inverting their intensities. Experimental results with two popular image dehazing techniques, applied to skin and retinal images, demonstrate the ability of this approach to enhance both image quality and the performance of lesion and vascular tree segmentation, respectively. Given the wide range of image dehazing techniques that can be straightforwardly adapted for illumination compensation purposes, the proposed approach enables an entire new set of simple and effective illumination compensation techniques.

Index Terms—Illumination Compensation, Image Dehazing, Skin Lesion Segmentation, Retinal Vessel Segmentation.

I. INTRODUCTION

MOVING illumination's influence is a central task in many image processing and computer vision problems. Many computer vision algorithms operate under the assumption that objects are lit by a single uniform light source. Unfortunately, this hypothesis is only realistic for ideal scenes where objects do not cast shadows nor present specularities, since they are planar, parallel to the image plane, opaque, and composed of materials that reflect light in a diffusive way.

However, in real world scenarios imaged under uncontrolled conditions, objects usually reflect light non-uniformly, resulting in low-quality images, due to a non-homogeneous reflectance and/or uneven illumination. In this case, low-level visual content such as colors, edges, or other local features

A. Galdran* and A. Campilho are with INESC TEC Porto, Portugal; e-mail: adrian.galdran@inesc.pt

A. Campilho is also with Faculdade de Engenharia, Universidade do Porto, Portugal; e-mail: campilho@fe.up.pt

A. Picon and A. Alvarez-Gila are with Tecnalia Research & Innovation, Spain; e-mails: {artzai.picon, aitor.alvarez}@tecnalia.com

A. Picon is also with Department of Control Engineering and Automatics at University of the Basque Country, e-mail: artzai.picon@ehu.eus

A. Bria, C. Marrocco, M. Molinara, and Francesco Tortorella are with the Dpt. of Electrical and Information Engineering, University of Cassino and L.M., Italy; e-mails: {a.bria, c.marrocco, m.molinara, tortorella}@unicas.it

Manuscript received August 17, 2017.

are degraded [1], negatively affecting computational image analysis techniques. Furthermore, illumination can influence a human observer, who will fixate better exposed regions while ignoring other areas suffering from irregular illumination [2]. It is often not feasible to acquire images under controlled illumination, and the most plausible alternative is then the use of post-processing tools to estimate the illumination field under which the scene was imaged, in order to remove its effect.

Let us consider a simplified model of image formation on a typical image acquisition device containing light receptors sensitive to long (λ_r), medium (λ_g), and short (λ_b) wavelengths, corresponding to red, green, and blue respectively. In this case, the triplet of values acquired by camera sensors is:

$$E(\lambda_c) = \int_{\Lambda} c(\lambda) \cdot R(\lambda) \cdot I(\lambda) d\lambda, \quad c \in \{r, g, b\} \quad (1)$$

where $c(\lambda)$ is the spectral sensitivity curve associated to the red, green, and blue filters inside the camera respectively, Λ is the visible spectrum, $I(\lambda)$ (irradiance, or illumination) describes the power distribution of the light source in the scene, $R(\lambda)$ is the spectral reflectance of an object, and $E(\lambda)$ is the intensity in the resulting image at wavelength λ .

Model (1) is only valid under certain assumptions, e.g. a single uniform source of light $I(\lambda)$. It also assumes that objects in the scene have isotropic diffusive reflectance $R(\lambda)$. By further considering spectral sensitivity functions $r(\lambda)$, $g(\lambda)$, and $b(\lambda)$ as δ -functions on the peak sensitivities λ_r , λ_g and λ_b [4], eq. (1) can be re-written as:

$$E(\lambda) = R(\lambda) \cdot I(\lambda), \quad \lambda \in \{\lambda_r, \lambda_g, \lambda_b\}. \quad (2)$$

The above model can only predict the values $\{E(\lambda_r), E(\lambda_g), E(\lambda_b)\}$ acquired by a camera assuming a uniform illumination equally affecting all pixels. Relaxing this hypothesis and considering a slowly-varying illumination field affecting each pixel in a different way, we obtain:

$$E(x, \lambda) = R(x, \lambda) \cdot I(x, \lambda), \quad \lambda \in \{\lambda_r, \lambda_g, \lambda_b\}. \quad (3)$$

Under the hypothesis that light color is neutral (*i.e.* if some standard white balancing is applied on the acquired image, which is usually the case in commercial cameras), the goal then becomes to solve for $R(x, \lambda)$ in the following equation:

$$E(x, \lambda) = R(x, \lambda) \cdot I(x), \quad \lambda \in \{\lambda_r, \lambda_g, \lambda_b\}. \quad (4)$$

We consider the problem of estimating illumination $I(x)$ at each x , and factorizing it out in eq. (4) for each color channel:

$$E(x) = R(x) \cdot I(x), \quad (5)$$

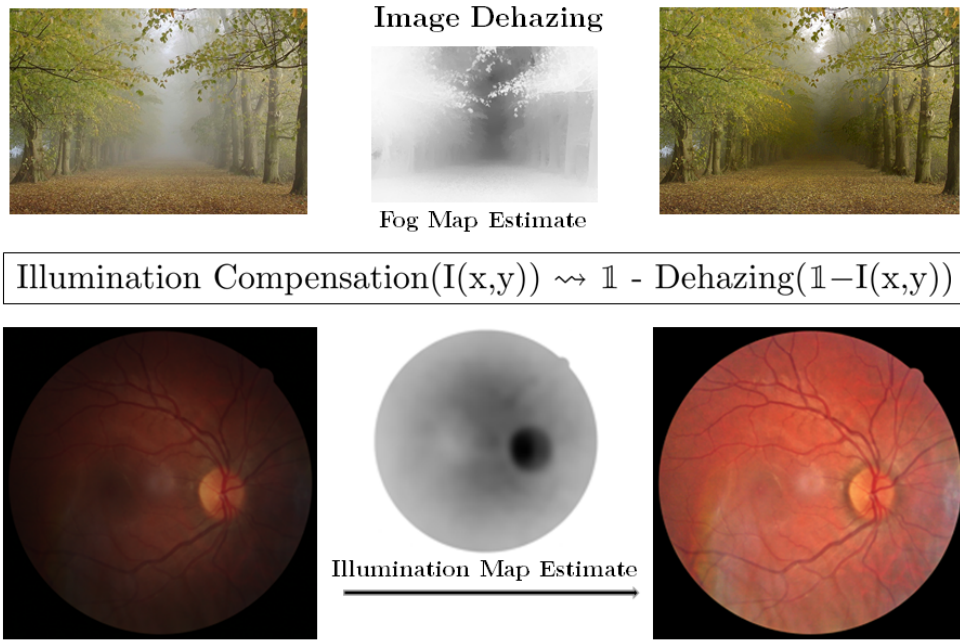


Fig. 1. The proposed methodology applied to correct illumination. In this case, the dehazing technique applied was [3]. For the hazy image, the estimated fog map is darker in the presence of degradation (fog), while for the under-exposed retinal image the illumination map is brighter in poorly-illuminated areas. Note that the optic disk and its surrounding area are estimated as the only well-illuminated regions.

71 where both $E(x)$ and $R(x)$ are color images and $I(x)$ is a
72 scalar image modeling a slowly-varying illumination field.

73 In order to estimate $I(x)$, many methods have been pro-
74 posed, *e.g.* based on wavelet-decompositions [5], histogram
75 transforms [6], or intrinsic image decomposition [7]. A promi-
76 nent family of techniques are derived from the Retinex theory
77 of color. It is important to note, however, that the standard
78 Retinex formulation solves the above problem in each color
79 channel, obtaining three separate illumination estimates. In
80 contrast, the technique proposed in this paper proceeds by
81 estimating a single illumination map for the entire image.

82 There is a wide range of computer vision applications that
83 can benefit from effective illumination compensation tech-
84 niques, *e.g.* image retrieval [8], remote sensing [9], dynamic
85 range compression [10], or simply producing a subjectively
86 more pleasant and natural-looking image [11]. In this work,
87 the focus is on specific applications in the medical imaging
88 field. In this context, some image modalities suffer from a
89 quality degradation produced by an artificial slowly-varying
90 illumination field that hinders visibility of anatomical struc-
91 tures of interest. This irregular illumination may appear due to
92 certain characteristics of the employed acquisition device, the
93 occlusion of ambient illumination, and/or the image formation
94 process itself. Removing this effect can lead to a substantial
95 increase in visual quality, as well as producing images better
96 suited for subsequent quantitative medical image analysis.

97 There is much interest on the biomedical imaging com-
98 munity in solving the problem of illumination compensation
99 adapted to different contexts. For instance, microscopy images
100 typically suffer from shading and non-uniform illumination,
101 due to defects in the image acquisition process, *e.g.* dirty
102 optics, vignetting, or camera non-linearities [12]. Different

103 solutions have been proposed, ranging from polynomial sur-
104 face fits to the image background to more complex methods
105 building an illumination model from a large image collection
106 [13]. Illumination correction is also useful for skin image
107 analysis [14], [15], often performed on images acquired by
108 standard cameras, sensitive to the ambient illumination. Yet
109 another relevant field of application is retinal fundus analysis.
110 Retinal images are typically acquired with a fundus camera,
111 an imaging device capable of illuminating and simultaneously
112 acquiring an image of the retina. Even if the image formation
113 process in this case will not obey most of the simplifying
114 assumptions that lead to the formulation of model (5), the il-
115 lumination inhomogeneities that often appear due to the three-
116 dimensional geometry of the eye and other potential artifacts
117 pose similar problems as in the standard optical photography
118 scenario. In this case, same anatomical structures, *e.g.* vascular
119 vessels, can suffer from spatially-varying brightness [16].

120 The remaining of the paper is organized as follows: the
121 image dehazing problem is introduced before establishing
122 a fundamental connection between the apparently unrelated
123 problems of fog removal and illumination correction, see fig.
124 1. This connection is validated through a statistical experiment
125 on a set of illumination-degraded and good-quality retinal
126 images. Two recent dehazing techniques are then re-casted
127 into illumination compensation operators and evaluated on a
128 set of skin and retinal fundus images. Quality improvement is
129 analyzed both in terms of objective quality scores and by ob-
130 serving the performance improvement of well-established skin
131 lesion and vessel tree segmentation methods after the proposed
132 illumination correction techniques are applied. We conclude by
133 discussing the results and future research directions.

134 II. ILLUMINATION COMPENSATION VIA IMAGE DEHAZING
135

136 The goal of image dehazing is to remove degradation in
137 images acquired under bad-weather conditions. In those cases,
138 atmospheric phenomena such as fog, dust, or haze, deflect light
139 trajectory, degrading the visual quality. Areas of the scene that
140 lie far away from the observer show faint colors, low saturation
141 and bright intensities. This physical effect was modeled in [17]
142 as being directly proportional to the distance of the object from
the observer, according to the following light propagation law:

$$H(x) = t(x)L(x) + A_\infty(1 - t(x)). \quad (6)$$

143 Here, $L(x)$ are the intensities that a camera would have
144 captured at a pixel location x , had the scene been acquired in a
145 haze-free scenario. However, when a degradation process due
146 to haze takes place, it results on the acquisition of a distorted
147 (hazy) representation of the scene $H(x)$. This degradation
148 process depends on two unknown quantities: $t(x)$, which is
149 the transmission of light in the atmosphere, inversely related
150 to the scene's depth, and A_∞ , the atmospheric light, a vectorial
151 quantity describing the predominant color of the atmosphere.

152 Following [18], we assume that image intensities are
153 normalized to $[0, 1]$, and $H(x)$ is white-balanced, *e.g.* the greatest
154 intensity in the image is white, and fog color can be estimated
155 by it, *i.e.*, $A_\infty = (1, 1, 1)$. Thus, model (6) simplifies to:

$$H(x) = t(x)L(x) + 1 - t(x). \quad (7)$$

156 The key observation is that fog and uneven illumination share
157 a common feature: both are low-frequency, slowly varying
158 phenomena. The main difference is that fog drives true colors
159 towards white, whereas a non-uniform illumination field drives
160 them towards darker intensities. We thus define the image
161 dehazing problem on the inverted intensity domain as the result
162 of considering model (7) on the image $1 - H(x)$. We also
163 define a solution to this problem as the result of solving the
164 image dehazing problem on the inverted intensity domain, and
165 then inverting again the intensities. These definitions, and the
166 assumptions made before eq. (7), lead to the following result:

167 **Theorem II.1.** *Solving the reflectance-illumination separation
168 problem in eq. (5) can be achieved by solving the image
169 dehazing problem on the inverted intensity domain.*

170 *Proof.* Finding a solution of the Image Dehazing problem
171 implies estimating the transmission $t(x)$, and then by simple
172 rearrangement, we directly obtain from eq. (7):

$$L(x) = \text{Dehazing}(H(x)) = \frac{H(x) - 1}{t(x)} + 1. \quad (8)$$

173 Suppose $L^0(x)$ is a solution for the Image Dehazing problem
174 in the inverted intensity domain. Then, $L^0(x)$ fulfills eq.
175 (8) applied to the inversion of $H(x)$ and inverted afterwards:

$$\begin{aligned} L^0(x) &= 1 - \text{Dehazing}(1 - H(x)) \\ &= 1 - \frac{(1 - H(x)) - 1}{t(x)} + 1 = \frac{H(x)}{t(x)}. \end{aligned} \quad (9)$$

176 Hence, $L^0(x)$ satisfies $H(x) = L^0(x)t(x)$. Here, $H(x)$ and
177 $L^0(x)$ are color images, while $t(x)$ is a slowly-varying scalar
178 image. Hence, $(L^0(x), t(x))$ is a solution of model (5). \square

This result leads to a general methodology to compensate
179 a low-frequency illumination field, consisting of three steps:
180

- 1) Given a image $H(x)$ corrupted by an uneven illumination,
181 invert its intensities $\tilde{H}(x) = 1 - H(x)$.
- 2) Select an image dehazing method M solving model (7),
183 *i.e.* mapping hazy images to haze-free ones.
- 3) Apply method M to $\tilde{H}(x)$, and invert the intensities of
185 the result, to produce an illumination-free image:
186

$$L(x) = 1 - M(\tilde{H}(x)). \quad (10)$$

In this work, we cast into illumination compensation techniques
187 two well-known image dehazing methods, the Dark
188 Channel [3] and the No-Black-Pixel-Constraint method [19].
189 Below we provide a short explanation of these techniques:
190

191 A. Dark Channel Image Dehazing (DC)
192

The Dark Channel Prior [3] is a popular fog removal method
193 based on a simple statistical observation of natural images:
most outdoor scenes contain colorful objects. Thus, given a
194 pixel x , a spatial neighborhood $\Omega(x)$ tends to contain low
195 intensity pixels in some of its chromatic components, *i.e.* the
196 *dark channel* of the image will contain mostly low values:
197

$$L^{\text{dark}}(x) = \min_{c \in \{R, G, B\}} \left(\min_{z \in \Omega(x)} L^c(z) \right) \approx 0. \quad (11)$$

This is not the case of hazy images. Even though pixels from
198 nearby regions will fulfill the dark channel prior, the additive
199 degradation component in eq. (6) remains, *i.e.*:
200

$$L^{\text{dark}}(x) \approx (1 - t(x))A_\infty. \quad (12)$$

Consequently, after estimation of the constant A_∞ , this allows
201 to approximate the distribution of haze in the scene as:
202

$$t(x) \approx 1 - \omega \left(\frac{L^{\text{dark}}(x)}{A_\infty} \right), \quad (13)$$

where ω is controls the amount of contrast introduced in the
203 final dehazed image. Due to the local depth constancy made
204 in eq. 13, the estimated transmission map usually suffers from
205 block artifacts, producing halos in the output image unless
206 removed. This can be accomplished with a refining filter, *e.g.*
207 the Guided Filter [20]. Once $t(x)$ and A_∞ are estimated, a
208 clean image is readily obtained by inverting eq. (6):
209

$$L(x) \approx \frac{H(x) - A_\infty(1 - t(x))}{t(x)}. \quad (14)$$

Relevant parameters for this method are the radius r of the
210 spatial neighborhood $\Omega(x)$ (square neighborhoods are usually
211 considered) and parameter ω controlling output contrast.
212

213 B. No Black Pixel Constraint Method (NBPC)
214

A different approach for estimating $t(x)$ is proposed in [18].
215 The refinement step required by the DC method is avoided by
216 robustly estimating local statistics of the atmospheric veil, defined
217 as the inverse of transmission $V(x) = 1 - t(x)$. Assuming
218 that $V(x)$ is smooth almost everywhere, the method imposes
219 two additional constraints on it: $V(x)$ must be positive, and it

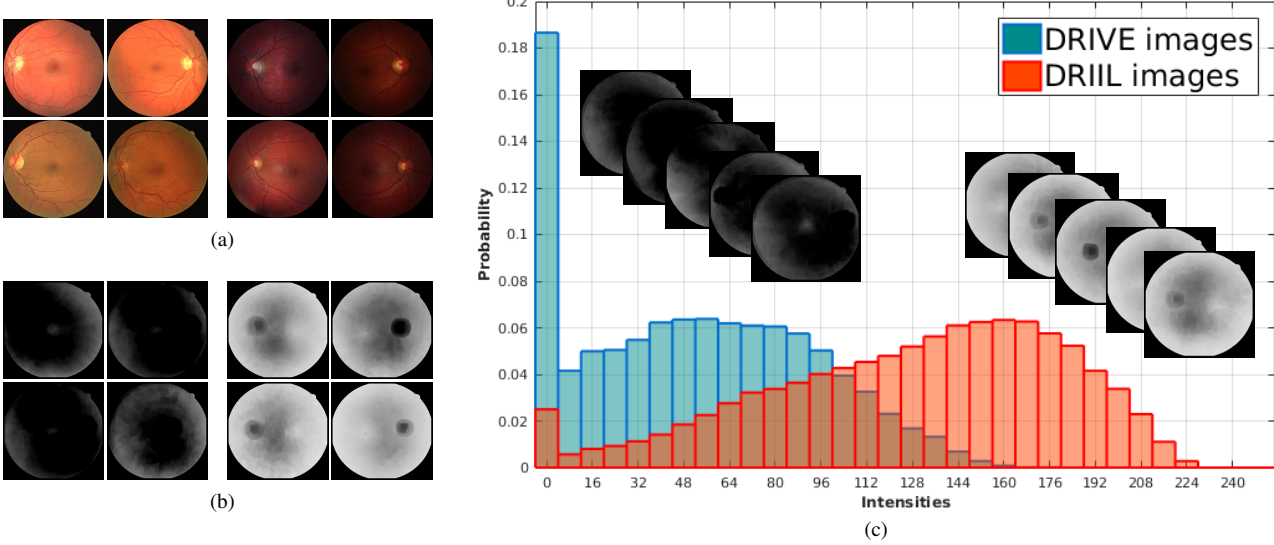


Fig. 2. (a) Images extracted from DRIVE (left) and DRIIL (right) (b) Dark Channel from inverted images (c) Histograms of the pixel intensities in every extracted Dark Channel (each bin contains counts for 8 intensity levels). Images were resized to a common resolution.

cannot be greater than the input intensity, *i.e.*, it is bounded between 0 and $I(x)$. $V(x)$ is estimated as the difference between local averages and local standard deviations across the image. A robust estimate of these quantities is achieved by employing the median instead of the mean, *i.e.*, considering $A(x) = \text{median}_r(H(x))$ as an estimate for the average in a region, and $B(x) = \text{median}_r(|H(x) - A(x)|)$ for the local standard deviation. With these estimates and the previous two constraints, the atmospheric veil can be approximated as:

$$V(x) = \max(\min(\omega \cdot B(x), H(x)), 0), \quad (15)$$

where r is the radius of neighborhoods around a pixel, and ω is a parameter specifying the amount of removed haze.

The above technique was extended in [19] with the additional No-Black-Pixel-Constraint, stating that local standard deviations of enhanced regions around a given pixel should be lower than its local average after the enhancement process. Although this constraint is formulated in terms of the unknown enhanced image $L(x)$, eq. (14) can be used to reformulate it in terms of $V(x)$, leading to the NBPC constraint:

$$V_r(x) \leq \text{mean}_r(H(x)) - \text{std}_r(H(x)). \quad (16)$$

After the atmospheric veil has been computed, a haze-free image is obtained by applying eq. (14) with $t(x) = 1 - V(x)$. Note that the most relevant parameters for the NBPC method remain the same as for the DC method, *i.e.*, radius r of the spatial neighborhoods and amount ω of desired contrast.

C. Statistical Justification

To empirically analyze the relationship between the presence of an uneven illumination field in an image and the presence of fog in its inverted counterpart, we conduct a statistical experiment. We first collect a set of well-contrasted, colorful retinal images from the DRIVE database [21]. Since this database is routinely employed to assess the performance of

retinal vessel extraction algorithms, we assume that it contains only good-quality samples. To obtain unevenly illuminated retinal images, we employ the DRIIL (Digital Retinal Images for ILLumination correction) database [22], which contains 165 retinal images acquired with a digital camera Canon EOS 40D attached to Canon CR-1 fundus camera. Some images from DRIVE and DRIIL are shown in Fig. (2a).

Next, we invert every image in both datasets, and compare their Dark Channel images following eq. (11), with a neighborhood size of $r = 20$. A sample of these Dark Channels is shown in Fig. (2b). If the Dark Channel detects smooth non-uniform illumination on inverted images, its average intensities should be low in case the retinal image does not suffer from this defect, while Dark Channels extracted from degraded images should contain higher intensities. This is confirmed by the results in Figs. (2a) and (2b). We also computed separate intensity histograms for both sets of images. Fig. (2c) shows both histograms overlaid. Note that pixels extracted from the field of view were considered. The statistical distribution of the intensities computed from DRIIL images is markedly different, with greater average-to-high intensity values. Also, a significant proportion of the low values observed in Dark Channels extracted from DRIIL images correspond to the optic disk region, usually free of shadows and illumination artifacts even when the image exhibits uneven illumination. These statistics support the applicability of dehazing techniques to reduce illumination artifacts from intensity-inverted images.

III. EXPERIMENTAL EVALUATION

In order to validate our approach for illumination compensation, extensive experimental analysis was performed on retinal and skin images. In both cases, first an objective image quality score was computed. Second, several popular image pre-processing algorithms were implemented, and their impact on a wide range of well-established algorithms for retinal vessel tree extraction and skin lesion segmentation was assessed.

285 **A. Data and Parameter Setting**

286 For assessing retinal image quality through an objective
 287 quality score, we employed the DRIIL database, introduced in
 288 Section II-C, in order to verify if the application of inverted
 289 dehazing was capable of improving visual quality. For retinal
 290 vessel segmentation, there is no database containing images
 291 with degraded illumination in combination with retinal vessel
 292 ground-truths. This is natural, since specialist's vessel delin-
 293 ection becomes hard under the presence of wrong illumination.
 294 To overcome this obstacle, we generated synthetic illumination
 295 fields extracted from the DRIIL database with a separate
 296 method, and cast them over images from the DRIVE database,
 297 which contains 40 good-quality images. DRIVE database
 298 also provides the corresponding ground-truth to evaluate the
 299 performance of vessel segmentation methods. Details of the
 300 image synthesis process are given in the next section.

301 Regarding skin imaging, we employed a set of 64 photo-
 302 graphs from the Dermatology Information System database
 303 [23] and 127 from the DermQuest database [24]. One hundred
 304 and eight images had melanomas, whereas 83 images had
 305 other skin lesions. These datasets have been used before to
 306 test uneven illumination removal techniques [14], [15], [25].
 307 For an objective quality score, we included results of a recently
 308 proposed quantitative quality assessment technique [26], mea-
 309 suring the degree of illumination uniformity on skin images.
 310 For skin lesion segmentation experiments, improvements in
 311 accuracy of a standard level set segmentation scheme when
 312 applied to the extraction of lesion borders was measured.

313 We tested the illumination compensation methods derived
 314 from the Dark Channel and the No Black Pixel Constrain
 315 methods (in the following, referred to as \widetilde{DC} and \widetilde{NBPC})¹.
 316 Spatial ratio and contrast parameters were set to default values
 317 of $r = 20$ and $\omega = 0.9$ and never changed through the
 318 experiments. For comparison with other image pre-processing
 319 techniques, we selected Multi-Scale Retinex (MSR) [27]
 320 (using the implementation provided in [28]), with default
 321 parameters (scales of 15, 80, and 250 pixels). In the case
 322 of the retinal vessel extraction problem, we included the
 323 Homomorphic Filtering, an illumination correction method
 324 that performs adequately on retinal images [29], and Contrast-
 325 Limited Adaptive Histogram Equalization [30], commonly
 326 used as a pre-processing step for retinal image analysis tasks
 327 [31]–[33]. CLAHE has been shown to perform effectively
 328 in the task of illumination compensation [29]. In the skin
 329 lesion segmentation problem, we also considered Multi-Stage
 330 Illumination Modeling (MSIM) [14], a method specifically
 331 designed to remove shadows from skin images.

332 **B. Experiments on Retinal Image Analysis**

333 *1) Objective Visual Quality Assessment:* For objectively
 334 assessing visual quality we computed the MSCN score [34] on
 335 every image from DRIIL after processing with \widetilde{DC} and \widetilde{NBPC}
 336 techniques. We also applied CLAHE, homomorphic filtering,
 337 and Retinex. MSCN is a quality metric for retinal images that

¹The corresponding source code to reproduce our results is made available at <https://github.com/agaldran/dehazing-for-illumination>.

TABLE I
 MSCN MEAN AND STANDARD DEVIATION SCORES ON THE DRIIL
 DATABASE FOR EACH METHOD. BEST SCORES PRINTED BOLD.

Method	None	MSR	Hom. Filt.	CLAHE	\widetilde{DC}	\widetilde{NBPC}
Mean	0.730	0.749	0.750	0.778	0.814	0.797
Std	0.104	0.023	0.090	0.018	0.024	0.042

proceeds by learning the appearance of a good and low-quality
 338 image through local Mean-Subtracted Contrast-Normalized
 339 statistics. It was trained on an independent proprietary dataset,
 340 and delivers a score in $[0, 1]$ indicating increasing visual
 341 quality. MSCN mean scores with standard deviation across
 342 the entire DRIIL database are given in Table I.

2) *Synthetic Data Generation:* In [35], a retinal image
 344 acquisition model composed of a luminosity and a contrast
 345 drift terms was built as:

$$I(x, y) = C(x, y)I^0(x, y) + L(x, y), \quad (17)$$

347 where $I(x, y)$ is the observed image of the eye fundus,
 348 $C(x, y)$, $L(x, y)$ represent respectively the contrast and lu-
 349 minosity distortion, and $I^0(x, y)$ is an improved version of
 350 $I(x, y)$. This method regularizes image intensities by imposing
 351 a Normal intensity distribution on the retinal background,
 352 in order to feed evenly distributed values to a subsequent
 353 automated diagnosis method. Thus, intensities of the output are
 354 not necessarily positive, nor do they have a visually mean-
 355 ingful interpretation. However, the contrast drift $C(x, y)$ can be
 356 considered as an estimate of the illumination field affecting the
 357 retina, and it can be employed to produce physically plausible
 358 synthetically degraded retinal images.

359 We applied eq. (17) to the entire DRIIL database, in
 360 order to learn an average illumination field template. Since
 361 the presence of the optic disk in the image conditions the
 362 shape of the illumination field, images in DRIIL were labeled
 363 according to its left or right position. Separate templates were
 364 extracted for both cases averaging $C(x, y)$ across left and
 365 right subclasses. This pair of illumination fields, which are
 366 denoted as *left-consensus-illumination* and *right-consensus-
 367 illumination*, are shown in Figs. (3b) and (3i). Both consensus
 368 illumination fields were then applied on the DRIVE database.
 369 For consistency with the illumination estimation phase, we
 370 again labeled DRIVE according to the position of the optic
 371 disk, and applied the corresponding consensus illumination to
 372 each image. An example of left and right-degraded DRIVE
 373 images is displayed in Figs. (3c) and (3j). It can be seen
 374 that corrupted images appear with a “natural” degradation:
 375 the optic disk is still the brightest region, and illumination
 376 smoothly decays towards the borders of the retina, consistently
 377 with the typical illumination decay due to the fundus camera
 378 illuminating perpendicularly the spherical geometry of the eye.
 379 The resulting set of images will be referred to as DRIVE-IL.

380 Finally, we applied to every image from DRIVE-IL CLAHE
 381 and homomorphic filtering, as well as the \widetilde{DC} and \widetilde{NBPC}
 382 techniques to attempt to remove these shadows. Examples of
 383 the application of these methods are also shown in Figs. (3d)
 384 to (3g) and Figs. (3k) to (3n).

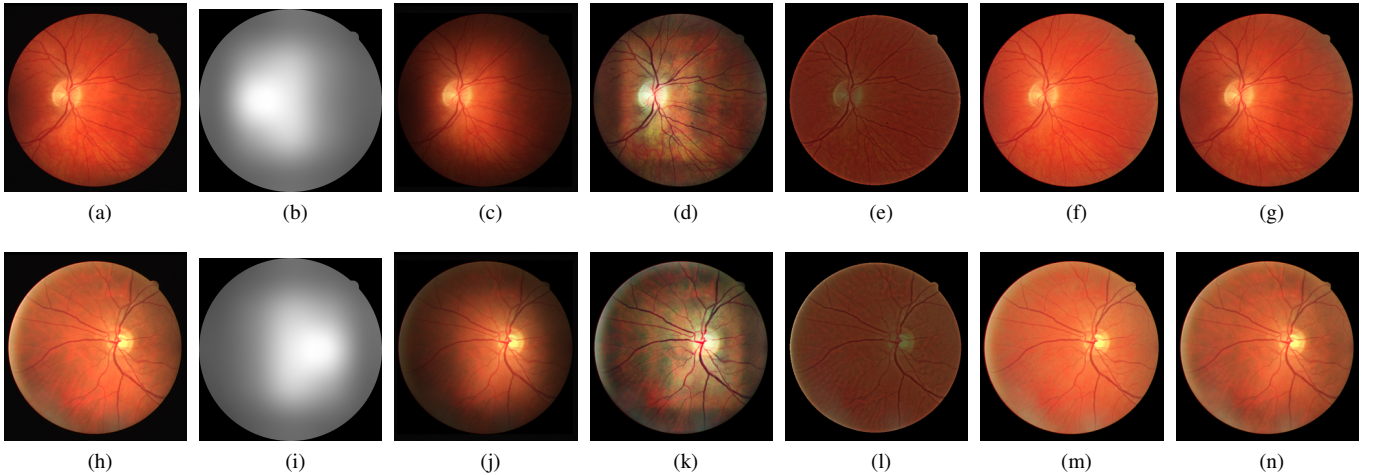


Fig. 3. (a) DRIVE image with optic disk to the left. (b) Left-consensus illumination extracted from DRIIL. (c) Corrupted image obtained by multiplying (a) and (b). (h) DRIVE image with optic disk to the right. (i) Right-consensus illumination extracted from DRIIL. (j) Corrupted image obtained by multiplying (g) and (h). (d)-(g), (k)-(n): Result of applying to (c), (i) methods: (d), (k): CLAHE; (e), (l): Homomorphic Filtering; (f), (m): NBPC; (g), (n): DC.

385 3) *Retinal Vessel Segmentation Evaluation*: To assess the
386 proposed approach for removing the unwanted effect of un-
387 even illumination, we tested several well-established vessel
388 segmentation methods on the DRIVE-IL database.

389 The following set of unsupervised vessel segmentation
390 techniques was considered: 1) **Nguyen et. al.** method [39]
391 computes pixel responses to line detectors at varying scales
392 and orientations. The output is built as a linear combination
393 of these responses. 2) **Azzopardi et. al.** method [32] is based
394 on COSFIRE (Combination Of Shifted Filter Responses). The
395 geometric mean of responses to a series of DoG filters is
396 computed, with shifting operations to add rotation invariance.
397 3) **Sum of top-hats'** technique enhances different vessel tree
398 portions by applying multiple morphological black top-hat
399 transforms at 12 different directions equally spaced in $[0, \pi]$.
400 Responses are summed together to yield the final result.

401 Supervised approaches were also included in our compari-
402 son. The following techniques were considered: 1) **Soares et.**
403 **al.** method [36] extracts from every pixel a set of responses to
404 Gabor-wavelet filters at multiple scales and supplies them to
405 a Bayesian classifier modeling vessel/non vessel likelihoods
406 as mixtures of Gaussians. 2) **Orlando et. al.** method [37]
407 builds on visual features extracted from several previous

408 techniques, e.g. [36] or [39], and features a fully-connected
409 Conditional Random Fields classifier, capable of dealing with
410 elongated structures. 3) **Liskowski et. al.** [38] technique builds
411 a Convolutional Neural Network that automatically learns
412 visual features from 27×27 pixel patches through a sequence
413 of feed-forward layers of convolutional filters interleaved with
414 nonlinear activation functions and pooling. Features are fed to
415 a sequence of fully connected layers that perform classifica-
416 tion. We use the BALANCED configuration from [38], where
417 the network is trained with equal proportion of classes.

418 Segmentation performances were evaluated on the 20 test
419 images of the DRIVE-IL database, with and without prepro-
420 cessing. All algorithms were configured to produce soft prob-
421 abilistic outputs. Receiving Operator Characteristics (ROC)
422 curves were computed with the true positive ratio (TPR)
423 versus the false positive ratio (FPR) with respect to a varying
424 threshold applied to the soft outputs. A close-up of the
425 resulting ROC curves is shown in Fig. 4 for typical sensitiv-
426 ity/specifity ranges ($\text{TPR} \geq 70\%$ and $1 - \text{FPR} \geq 90\%$). To
427 quantify performance, the area under the ROC curve (AUC)
428 was calculated, where $\text{AUC} = 1$ represents a perfect segmen-
429 tation. The resulting AUC values are reported in Table II for all
430 segmentation algorithms and different preprocessing methods.

TABLE II
AUC% PERFORMANCES OF VESSEL SEGMENTATION APPLIED TO DRIVE-IL w/o PROCESSING AND AFTER PROCESSING w/ HOMOMORPHIC FILTERING (HF), CLAHE (CL), DARK CHANNEL ON INVERTED INTENSITIES (DC), AND NBPC ON INVERTED INTENSITIES (NBPC). PERFORMANCE ON DRIVE IS ALSO GIVEN IN THE LAST COLUMN FOR REFERENCE. THE TWO HIGHEST PERFORMANCES IN EACH ROW ARE PRINTED IN BOLD.

Method	DRIVE-IL	DRIVE-IL + HF	DRIVE-IL + CL	DRIVE-IL + DC	DRIVE-IL + NBPC	DRIVE
Soares et. al. – [36]	95.51	95.69	95.72	96.01	95.89	96.09
Orlando et. al. – [37]	94.88	95.80	93.78	95.29	95.24	95.27
Liskowski et. al. – [38]	96.76	97.35	97.20	97.15	97.09	97.07
Azzopardi et. al. – [32]	93.58	93.76	94.32	94.99	94.99	95.24
Nguyen et. al. – [39]	93.16	91.44	92.97	93.57	93.09	93.52
Sum of Top-Hats – ΣTH	88.24	92.05	91.65	93.71	93.35	93.79

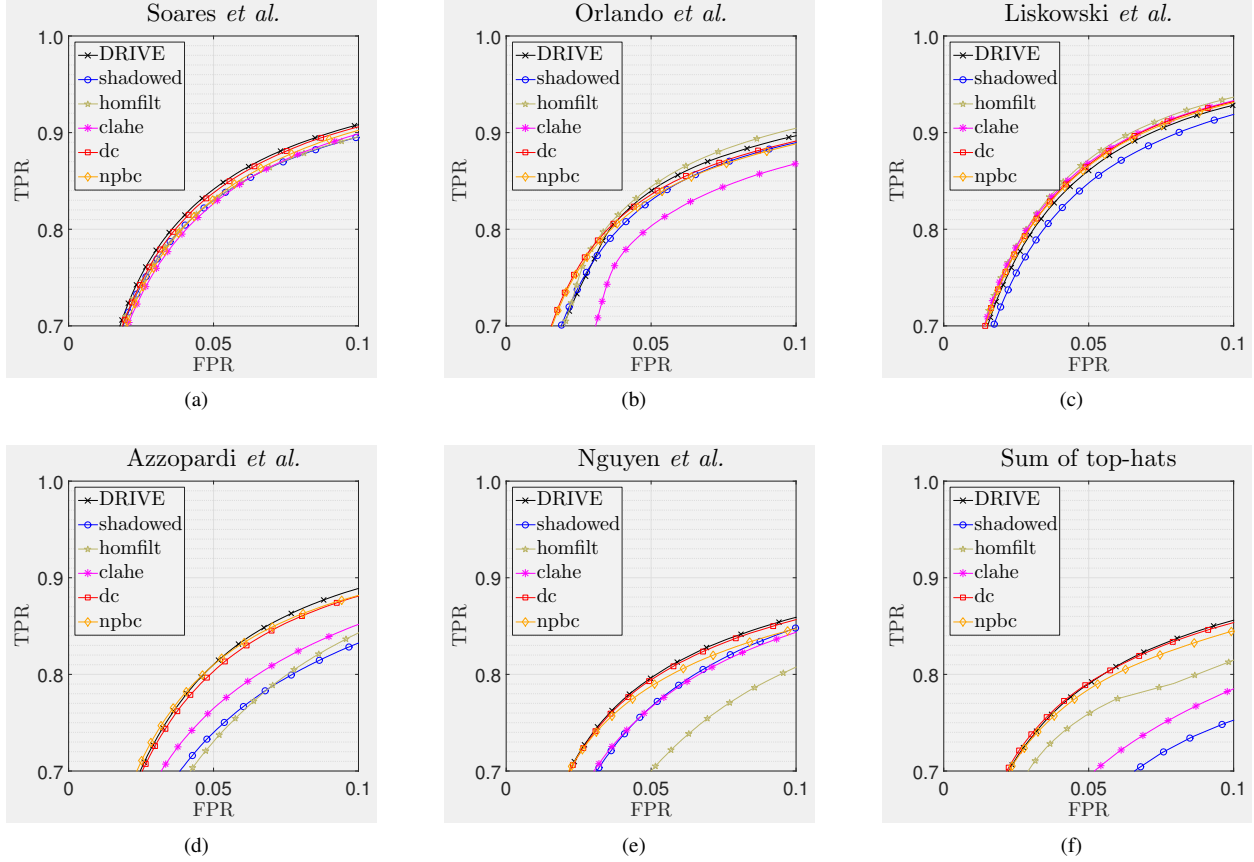


Fig. 4. Partial ROC curves of six vessel tree segmentation algorithms applied to the test images in DRIVE and to the test images in DRIVE-IL w/o processing (shadowed) and after processing w/ homomorphic filtering (homfilt), CLAHE (clahe), DC (dc), and NBPC (npbc).

To determine statistically significantly differences in AUC, we applied the bootstrap procedure [40] as follows: the test set was randomly sampled with replacement 1,000 times so that each new set of sampled data contained the same number of examples as the original set. For each preprocessing method M_i , differences in AUC between M_i and $M_{j,j \neq i}$ were computed as $\Delta\text{AUC}(M_i, M_j) = \text{AUC}(M_i) - \text{AUC}(M_j)$. Resampling 1,000 times resulted in 1,000 values for $\Delta\text{AUC}(M_i, M_j)$. P -values were defined as the fraction of $\Delta\text{AUC}(M_i, M_j)$ values being negative or zero, corresponding to cases in which M_i performed worse than or equal to M_j .

The statistical significance level was chosen as $\alpha = 0.05$ but, due to the number of comparisons $m > 1$, we applied the Bonferroni correction [41]. Thus, performance differences were considered statistically significant if $p < \alpha/m$. In Table III, we report all possible $m = 10$ comparisons between the preprocessing methods considered. According to the Bonferroni correction, differences were significant if $p < 0.005$.

C. Experiments on Skin Image Analysis

The problem of illumination compensation on skin images is considered now.

TABLE III
AUC% PERFORMANCE DIFFERENCES OF VESSEL SEGMENTATION APPLIED TO IMAGES IN DRIVE-IL W/O PROCESSING (**SH**) AND AFTER PROCESSING W/ HOMOMORPHIC FILTERING (**HF**), CLAHE (**CL**), $\widetilde{\text{DC}}$ (**DC**), AND NBPC (**NB**). STATISTICALLY SIGNIFICANTLY DIFFERENCES PRINTED IN BOLD.

Method	HF-SH	CL-SH	DC-SH	NB-SH	HF-CL	DC-HF	DC-CL	DC-NB	NB-HF	NB-CL
Soares <i>et. al.</i> – [36]	+0.18	+0.21	+0.50	+0.38	+0.03	+0.32	+0.29	+0.12	+0.20	+0.17
Orlando <i>et. al.</i> – [37]	+0.92	-1.10	+0.41	+0.36	+2.02	-0.51	+1.51	+0.05	-0.56	+1.47
Liskowski <i>et. al.</i> – [38]	+0.59	+0.44	+0.39	+0.34	+0.15	-0.20	-0.05	+0.05	-0.25	-0.10
Azzopardi <i>et. al.</i> – [32]	+0.19	+0.74	+1.41	+1.41	-0.56	+1.22	+0.67	+0.001	+1.22	+0.67
Nguyen <i>et. al.</i> – [39]	-1.72	-0.19	+0.41	-0.07	-1.53	+2.14	+0.61	+0.48	+1.66	+0.13
Sum of Top-Hats – ΣTH	+3.81	+3.41	+5.48	+5.11	+0.39	+1.67	+2.06	+0.36	+1.30	+1.70

TABLE IV
AGIC MEAN AND STANDARD DEVIATION SCORES ON THE CONSIDERED DATABASE FOR EACH METHOD. BEST SCORES PRINTED BOLD.

Method	None	MSR	MSIM	\widetilde{DC}	\widetilde{NBPC}
Mean AGIC	0.1432	0.1276	0.1291	0.1000	0.1001
Std AGIC	0.1067	0.0769	0.0830	0.0781	0.1312

452 1) *Objective Visual Quality Assessment*: First, for an objective 453 evaluation of visual quality, we compare \widetilde{DC} and \widetilde{NBPC} to the result obtained with MSR and MSIM, employing the 454 Average Gradient of Illumination Component (AGIC) score 455 [26]. AGIC measures illumination distortion as the difference 456 of mean values between adjacent patches on the image. For 457 that, the image is first divided into $M \times N$ blocks, and the 458 maximum difference between averaged intensities on a block 459 with respect to its neighboring blocks (normalized by the 460 average intensity in the considered block) is computed. All 461 block scores are finally averaged across the entire image. A 462 lower value indicates that a more uniform illumination affects 463 the image. The mean/standard deviation AGIC scores on the 464 considered database, with a square block of side 200 pixels, 465 for \widetilde{DC} , \widetilde{NBPC} , MSR and MSIM are given in Table IV. 466

2) *Skin Lesion Segmentation Evaluation*: We now apply the Chan-Vese segmentation method in its RGB version [42] (as implemented in [43]) to the considered database. This method minimizes the following energy:

$$E(C, c_1, c_2) = \mu \cdot \text{Length}(C) + \nu \cdot \text{Area}(\text{in}(C)) + \lambda_1 \int_{\text{in}(C)} |I(x) - c_1| + \lambda_2 \int_{\text{out}(C)} |I(x) - c_2|, \quad (18)$$

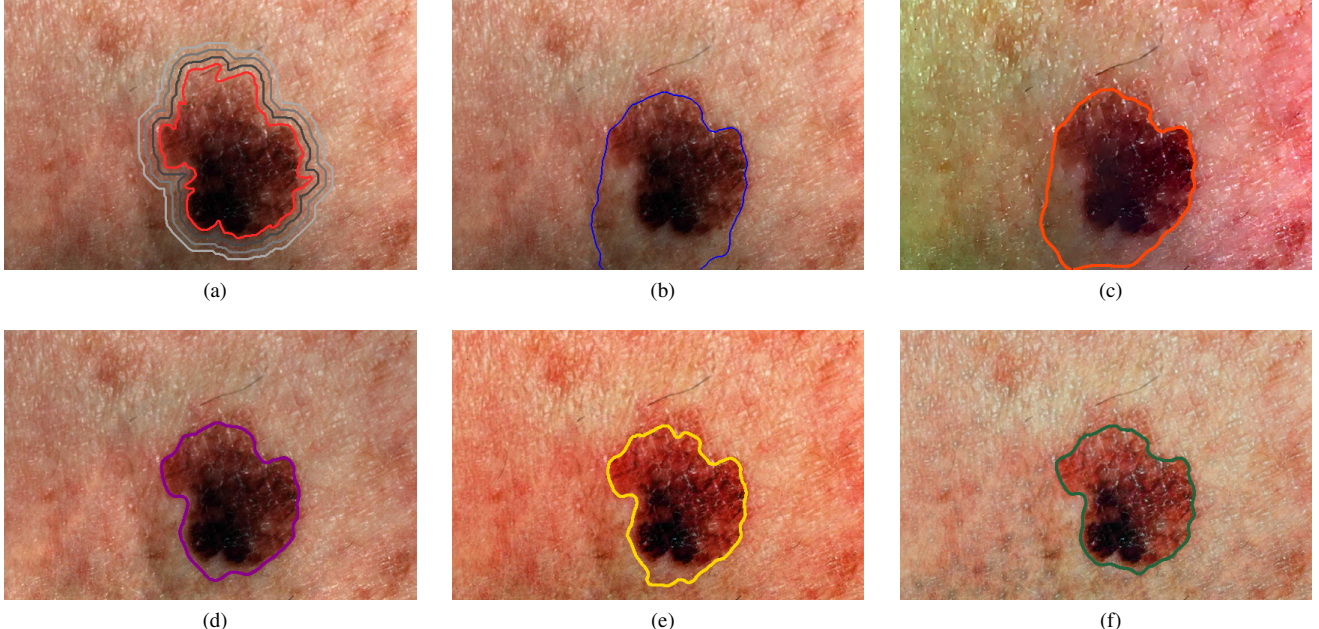


Fig. 5. (a) Part of the set of initializations employed to apply model (18) (diameter expansion factors of 1.05%, 1.10% and 1.15% from the original groundtruth, depicted in red), and segmentation results corresponding to the largest initialization, after correcting the original image with the methods (b) None (c) MSR [27] (d) MSIM [14] (e) \widetilde{NBPC} (f) \widetilde{DC} .

where $I(x), c_1, c_2 \in \mathbb{R}^3$, C is the border of the segmentation, and $\text{in}(C), \text{out}(C)$ are the inner and outer regions in which C separates the image. This model has been employed for skin image segmentation in the past [44], [45]. After pre-processing each image with the different considered techniques, eq. (18) was run with the baseline parameters provided in the referred implementation, i.e., $\mu = 0.25$, $\nu = 0$, $\lambda_1 = \lambda_2 = 1$. 467
468
469
470
471
472
473

Automatically generating appropriate initializations for level-set methods is an open research area [46], beyond the scope of this work. Thus, as an initialization for the minimization process, the provided ground-truth binary masks were morphologically dilated to obtain a set of progressively larger masks surrounding the lesion. Successive expansions of the manual segmentation were produced in terms of percentages of the maximum diameter of the segmented lesion: from 105% to 115% dilations, sampling each 1%. A set of 10 initializations was generated, as in Fig. (5a). For each initial contours, model (18) was run until convergence for each technique. 474
475
476
477
478
479
480
481
482
483
484

Initializations further away from true segmentations will progressively degrade the performance of method (18). This degradation can be measured in terms of Hausdorff distance [47]. Rather than observing the overlap between segmentation and groundtruth through a false/true positive/negative pixel count, Hausdorff distance measures how different the boundary of the segmentation and the true boundary are. This is meaningful for skin lesion analysis, since most automatic classification systems need fine information of the lesion's shape, its symmetry, or diameter [48], to precisely diagnose lesions. The result of these experiments is shown in Fig. 6, for 5000 randomly generated bootstrap iterations. Uncertainty bands represent a 25% confidence interval around the mean Hausdorff error across the entire image database. 485
486
487
488
489
490
491
492
493
494
495
496
497
498

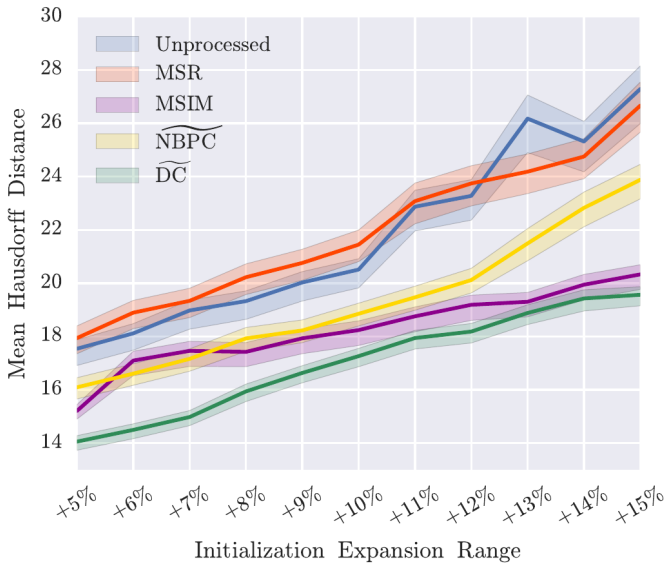


Fig. 6. Hausdorff distances for all methods, progressively larger initializations.

499

IV. DISCUSSION

500 For retinal images, Table I showed that illumination compensation by inverted dehazing substantially improved MSCN
 501 scores with respect to original images. This was confirmed in
 502 the vessel segmentation analysis of Table III. Compared to the
 503 unprocessed DRIVE-IL dataset, all 6 segmentation algorithms
 504 improved performance, with DC ($\Delta AUC\% = +1.43$), 5 of 6
 505 improved with NBPC ($\Delta AUC\% = +1.26$), 5 of 6 improved
 506 with HF ($\Delta AUC\% = +0.66$), and 4 of 6 improved with
 507 CLAHE ($\Delta AUC\% = +0.59$). Remarkably, dehazing-based
 508 methods DC and NBPC never resulted in a performance
 509 deterioration, whereas this happened in 1 case with HF and
 510 in 2 cases with CLAHE. This indicates that both proposed
 511 techniques result in a more robust illumination compensation.
 512

513 On the other hand, results of DC were slightly superior to
 514 those of NBPC ($\Delta AUC\% = +0.18$) in 5 cases and greatly
 515 outperformed those of CLAHE ($\Delta AUC\% = +0.85$) in 5
 516 cases and those of HF ($\Delta AUC\% = +0.77$) in 4 cases. This
 517 confirms a slight superiority of DC with respect to NBPC in
 518 the illumination correction task for retinal images.

519 It is important to stress that the 3 supervised methods, which
 520 also achieved the highest absolute performance, performed
 521 equally on DRIVE, DRIVE-IL+DC, and DRIVE-IL+NBPc.
 522 This suggests that illumination compensation by inverted
 523 dehazing represents an effective method to correct uneven
 524 illumination. Performance of supervised approaches raises to
 525 the same levels exhibited in undegraded images when both DC
 526 and NBPC are applied to a corrupted set of images, thereby
 527 strongly supporting our illumination correction approach.

528 In the skin imaging case, results from an image quality
 529 metric specifically developed to assess illumination uniformity
 530 on this class of images were reported in Table IV for a wide set
 531 of images processed with each of the considered techniques. It
 532 can be appreciated that illumination variability across images
 533 was better reduced, both in terms of average and standard
 534 deviation, by the DC method. In terms of the AGIC score,

the remaining methods (NBPC, MSIM, and MSR) performed
 535 slightly worse, all of them scoring similarly, always improving
 536 illumination uniformity with respect to the original images.
 537 Regarding the skin lesion segmentation problem depicted in
 538 Fig. 5, as expected none of the considered pre-processing
 539 methods preserves their performance as the distance from
 540 the initialization to the ground-truth segmentation increases.
 541 This initialization dependency is a common problem of active
 542 contours techniques. However, results shown in Fig. (6) also
 543 indicate a clear tendency of MSIM, NBPC and DC to reduce
 544 this dependency, which is a much desirable feature for any pre-
 545 processing approach. It can be appreciated that pre-processing
 546 the images with MSR and omitting any pre-processing leads to
 547 an overall approximate increase of 10 mean Hausdorff distance
 548 error points when the initialization expansion range increases
 549 by 10% with respect to the initial size. This performance
 550 degradation is reduced by the other three considered pre-
 551 processing methods, specially by MSIM, and DC.

552 Finally, Fig. (6) also shows that as the distance from the
 553 ground-truth increases, the performance of NBPC degrades,
 554 approaching that of MSR. This is avoided by MSIM and DC,
 555 which perform on par and converge to similar error increments
 556 after distance has increased in 10% from its initial value. This
 557 error increments reduce to approximately half of the increment
 558 produced by the other methods. Furthermore, the confidence
 559 bands associated with these two techniques are considerably
 560 narrower, suggesting that MSIM and DC can fulfill the task
 561 of illumination compensation more robustly.

V. CONCLUSIONS

562 In this work we have theoretically and empirically demon-
 563 strated the potential of image dehazing techniques for the task
 564 of illumination correction, when applied on the inverted inten-
 565 sity domain. We have applied two well-established fog removal
 566 methods on two different medical image applications, namely
 567 skin images and retinal images of the eye fundus. This pre-
 568 processing has been evaluated for the task of lesion and retinal
 569 vessel segmentation respectively, comparing performance to
 570 popular techniques through extensive numerical experiments.
 571 These experiments verify that inverted image dehazing tech-
 572 niques represent powerful illumination correction techniques.

VI. ACKNOWLEDGMENTS

573 This work is financed by the European Regional Develop-
 574 ment Fund through the Operational Programme for Com-
 575 petitiveness and Internationalisation - COMPETE 2020 Pro-
 576 gramme, and by the FCT - Fundação para a Ciência e a
 577 Tecnologia within project CMUP-ERI/TIC/0028/2014.

578 This work has also been partially supported by the Ecsel
 579 Project Astonish (contract 692470) funded by the EC and the
 580 Spanish Ministry of Energy, Tourism and Digital Agenda, and
 581 by the Elkarte program/Project Melamic2 (KK-2017/00041)
 582 funded by Basque Government, Industry Department.

REFERENCES

- [1] V. Vonikakis, R. Kouskouridas, and A. Gasteratos, "On the evaluation of illumination compensation algorithms," *Multimedia Tools and Applications*, pp. 1–21, May 2017.

- [2] F. Hermens and S. Zdravković, "Information extraction from shadowed regions in images: An eye movement study," *Vision Research*, vol. 113, Part A, pp. 87–96, Aug. 2015.
- [3] K. He, J. Sun, and X. Tang, "Single Image Haze Removal Using Dark Channel Prior," *IEEE Transactions on Pattern Analysis and Machine Intelligence*, vol. 33, no. 12, pp. 2341–2353, Dec. 2011.
- [4] M. Bertalmío, *Image Processing for Cinema*, 1st ed. Boca Raton: Chapman and Hall/CRC, Feb. 2014.
- [5] C. Jung, Q. Yang, T. Sun, Q. Fu, and H. Song, "Low light image enhancement with dual-tree complex wavelet transform," *Visual Communication and Image Representation*, vol. 42, pp. 28–36, Jan. 2017.
- [6] P. H. Lee, S. W. Wu, and Y. P. Hung, "Illumination Compensation Using Oriented Local Histogram Equalization and its Application to Face Recognition," *IEEE Transactions on Image Processing*, vol. 21, no. 9, pp. 4280–4289, Sep. 2012.
- [7] M. F. Tappen, W. T. Freeman, and E. H. Adelson, "Recovering intrinsic images from a single image," *IEEE Transactions on Pattern Analysis and Machine Intelligence*, vol. 27, no. 9, pp. 1459–1472, Sep. 2005.
- [8] S. R. Dubey, S. K. Singh, and R. K. Singh, "A multi-channel based illumination compensation mechanism for brightness invariant image retrieval," *Multimedia Tools and Applications*, vol. 74, no. 24, pp. 11223–11253, Dec. 2015.
- [9] M. S. Al-Rawi, A. Galdran, X. Yuan, M. Eckert, J. F. Martinez, F. Elmgren, B. Cürkülu, J. Rodriguez, J. Bastos, and M. Pinto, "Intensity normalization of sidescan sonar imagery," in *2016 Sixth International Conference on Image Processing Theory, Tools and Applications (IPTA)*, Dec. 2016, pp. 1–6.
- [10] M. Ogata, T. Tsuchiya, T. Kubozono, and K. Ueda, "Dynamic range compression based on illumination compensation," *IEEE Transactions on Consumer Electronics*, vol. 47, no. 3, pp. 548–558, Aug. 2001.
- [11] S. Wang, J. Zheng, H. M. Hu, and B. Li, "Naturalness Preserved Enhancement Algorithm for Non-Uniform Illumination Images," *Transactions on Image Processing*, vol. 22, no. 9, pp. 3538–3548, Sep. 2013.
- [12] Likar, Maintz, Viergever, and Pernuš, "Retrospective shading correction based on entropy minimization," *Journal of Microscopy*, vol. 197, no. 3, pp. 285–295, Mar. 2000.
- [13] K. Smith, Y. Li, F. Piccinini, G. Csucs, C. Balazs, A. Bevilacqua, and P. Horvath, "CIDRE: an illumination-correction method for optical microscopy," *Nature Methods*, vol. 12, no. 5, pp. 404–406, May 2015.
- [14] J. Glaister, R. Amelard, A. Wong, and D. A. Clausi, "MSIM: Multistage Illumination Modeling of Dermatological Photographs for Illumination-Corrected Skin Lesion Analysis," *IEEE Transactions on Biomedical Engineering*, vol. 60, no. 7, pp. 1873–1883, Jul. 2013.
- [15] Z. Liu and J. Zerubia, "Skin image illumination modeling and chromophore identification for melanoma diagnosis," *Physics in Medicine and Biology*, vol. 60, no. 9, p. 3415, 2015.
- [16] Y. Zheng, B. Vanderbeek, R. Xiao, E. Daniel, D. Stambolian, M. Maguire, J. O'Brien, and J. Gee, "Retrospective illumination correction of retinal fundus images from gradient distribution sparsity," in *2012 9th IEEE International Symposium on Biomedical Imaging (ISBI)*, May 2012, pp. 972–975.
- [17] H. Koschmieder, *Theorie der horizontalen Sichtweite: Kontrast und Sichtweite*. Keim & Nemnich, 1925.
- [18] J. P. Tarel and N. Hautiere, "Fast visibility restoration from a single color or gray level image," in *2009 IEEE 12th International Conference on Computer Vision*, Sep. 2009, pp. 2201–2208.
- [19] J. P. Tarel, N. Hautiere, L. Caraffa, A. Cord, H. Halmaoui, and D. Gruyer, "Vision Enhancement in Homogeneous and Heterogeneous Fog," *IEEE Intelligent Transportation Systems*, vol. 4, no. 2, pp. 6–20, 2012.
- [20] K. He, J. Sun, and X. Tang, "Guided Image Filtering," *IEEE Transactions on Pattern Analysis and Machine Intelligence*, vol. 35, no. 6, pp. 1397–1409, Jun. 2013.
- [21] J. J. Staal, M. D. Abramoff, M. Niemeijer, M. A. Viergever, and B. v. Ginneken, "Ridge based vessel segmentation in color images of the retina," *IEEE Transactions on Medical Imaging*, vol. 23, no. 4, pp. 501–509, 2004.
- [22] R. Kolar, J. Odstrcilik, J. Jan, and V. Harabis, "Illumination correction and contrast equalization in colour fundus images," in *2011 19th European Signal Processing Conference*, Aug. 2011, pp. 298–302.
- [23] "DermIS," Dec. 2016. [Online]. Available: www.dermis.net.
- [24] "DermQuest," Dec. 2016. [Online]. Available: www.dermquest.com.
- [25] P. G. Cavalcanti and J. Scharcanski, "Automated prescreening of pigmented skin lesions using standard cameras," *Computerized Medical Imaging and Graphics*, vol. 35, no. 6, pp. 481–491, Sep. 2011.
- [26] Y. Lu, F. Xie, Y. Wu, Z. Jiang, and R. Meng, "No Reference Uneven Illumination Assessment for Dermoscopy Images," *IEEE Signal Processing Letters*, vol. 22, no. 5, pp. 534–538, May 2015.
- [27] D. J. Jobson, Z. Rahman, and G. A. Woodell, "A multiscale retinex for bridging the gap between color images and the human observation of scenes," *IEEE Transactions on Image Processing*, vol. 6, no. 7, pp. 965–976, Jul. 1997.
- [28] A. B. Petro, C. Sbert, and J.-M. Morel, "Multiscale Retinex," *Image Processing On Line*, pp. 71–88, Apr. 2014. [Online]. Available: <http://www.ipol.im/pub/art/2014/107/>
- [29] S. H. Rasta, M. E. Partovi, H. Seyedarabi, and A. Javadzadeh, "A Comparative Study on Preprocessing Techniques in Diabetic Retinopathy Retinal Images: Illumination Correction and Contrast Enhancement," *Journal of Medical Signals and Sensors*, vol. 5, no. 1, pp. 40–48, 2015.
- [30] S. M. Pizer, E. P. Amburn, J. D. Austin, R. Cromartie, A. Geselowitz, T. Greer, B. ter Haar Romeny, J. B. Zimmerman, and K. Zuiderweld, "Adaptive histogram equalization and its variations," *Computer Vision, Graphics, and Image Processing*, vol. 39, no. 3, pp. 355–368, Sep. 1987.
- [31] M. H. A. Fadzil, H. A. Nugroho, H. Nugroho, and I. L. Iznita, "Contrast Enhancement of Retinal Vasculature in Digital Fundus Image," in *Int. Conf. on Digital Image Processing*, Mar. 2009, pp. 137–141.
- [32] G. Azzopardi, N. Strisciuglio, M. Vento, and N. Petkov, "Trainable COS-FIRE filters for vessel delineation with application to retinal images," *Medical Image Analysis*, vol. 19, no. 1, pp. 46–57, Jan. 2015.
- [33] J. I. Orlando, E. Prokofyeva, M. del Fresno, and M. Blaschko, "Convolutional Neural Network Transfer for Automated Glaucoma Identification," in *12th International Symposium on Medical Information Processing and Analysis*. SPIE, Dec. 2016.
- [34] A. Galdran, T. Araújo, A. Mendonça, and A. Campilho, "Retinal Image Quality Assessment by Mean-Subtracted Contrast-Normalized Coefficients," in *Computational Vision and Medical Image Processing VI, 6th ECCOMAS Thematic Conference on Computational Vision and Medical Image Processing - VipIMAGE 2017*. CRC Press, Oct. 2017.
- [35] M. Foracchia, E. Grisan, and A. Ruggeri, "Luminosity and contrast normalization in retinal images," *Medical Image Analysis*, vol. 9, no. 3, pp. 179–190, Jun. 2005.
- [36] J. V. B. Soares, J. J. G. Leandro, R. M. Cesar, H. F. Jelinek, and M. J. Cree, "Retinal vessel segmentation using the 2-D Gabor wavelet and supervised classification," *IEEE Transactions on Medical Imaging*, vol. 25, no. 9, pp. 1214–1222, Sep. 2006.
- [37] J. I. Orlando, E. Prokofyeva, and M. B. Blaschko, "A Discriminatively Trained Fully Connected Conditional Random Field Model for Blood Vessel Segmentation in Fundus Images," *IEEE Transactions on Biomedical Engineering*, vol. 64, no. 1, pp. 16–27, Jan. 2017.
- [38] P. Liskowski and K. Krawiec, "Segmenting Retinal Blood Vessels With Deep Neural Networks," *IEEE Transactions on Medical Imaging*, vol. 35, no. 11, pp. 2369–2380, Nov. 2016.
- [39] U. T. V. Nguyen, A. Bhuiyan, L. A. F. Park, and K. Ramamohanarao, "An effective retinal blood vessel segmentation method using multi-scale line detection," *Pattern Recognition*, vol. 46, no. 3, pp. 703–715, 2013.
- [40] F. W. Samuelson and N. Petrick, "Comparing image detection algorithms using resampling," in *IEEE ISBI*, 2006, pp. 1312–1315.
- [41] O. J. Dunn, "Multiple Comparisons Among Means," *Journal of the American Statistical Association*, vol. 56, no. 293, pp. 52–64, 1961.
- [42] T. F. Chan, B. Y. Sandberg, and L. A. Vese, "Active Contours without Edges for Vector-Valued Images," *Journal of Visual Communication and Image Representation*, vol. 11, no. 2, pp. 130–141, Jun. 2000.
- [43] P. Getreuer, "Chan-Vese Segmentation," *Image Processing On Line*, vol. 2, pp. 214–224, Aug. 2012. [Online]. Available: <http://www.ipol.im/pub/art/2012/g-cv/>
- [44] M. Silveira, J. C. Nascimento, J. S. Marques, A. R. S. Marcal, T. Mendonça, S. Yamauchi, J. Maeda, and J. Rozeira, "Comparison of Segmentation Methods for Melanoma Diagnosis in Dermoscopy Images," *IEEE Journal of Selected Topics in Signal Processing*, vol. 3, no. 1, pp. 35–45, Feb. 2009.
- [45] P. G. Cavalcanti, J. Scharcanski, L. E. D. Persia, and D. H. Milone, "An ICA-based method for the segmentation of pigmented skin lesions in macroscopic images," in *IEEE Int. Conf. Engineering in Medicine and Biology Society*, Aug. 2011, pp. 5993–5996.
- [46] Q. Liu, M. Jiang, P. Bai, and G. Yang, "A novel level set model with automated initialization and controlling parameters for medical image segmentation," *Computerized Medical Imaging and Graphics*, vol. 48, pp. 21–29, Mar. 2016.
- [47] V. Chalana and Y. Kim, "A methodology for evaluation of boundary detection algorithms on medical images," *IEEE Transactions on Medical Imaging*, vol. 16, no. 5, pp. 642–652, Oct. 1997.
- [48] N. R. Abbasi, H. M. Shaw, D. S. Rigel, R. J. Friedman, W. H. McCarthy, I. Osman, A. W. Kopf, and D. Polksky, "Early Diagnosis of Cutaneous Melanoma: Revisiting the ABCD Criteria," *JAMA*, vol. 292, no. 22, pp. 2771–2776, Dec. 2004.